

High-performance flexible p-type Ce-filled $\text{Fe}_3\text{CoSb}_{12}$ skutterudite thin film for medium-to-high-temperature applications

Received: 14 March 2024

Accepted: 10 May 2024

Published online: 18 May 2024

Check for updates

Dou Li^{1,4}, Xiao-Lei Shi^{2,4}, Jiayi Zhu¹, Tianyi Cao², Xiao Ma¹, Meng Li², Zhuokun Han³, Zhenyu Feng¹, Yixing Chen¹, Jianyuan Wang³, Wei-Di Liu², Hong Zhong¹✉, Shuangming Li¹✉ & Zhi-Gang Chen²✉

P-type $\text{Fe}_3\text{CoSb}_{12}$ -based skutterudite thin films are successfully fabricated, exhibiting high thermoelectric performance, stability, and flexibility at medium-to-high temperatures, based on preparing custom target materials and employing advanced pulsed laser deposition techniques to address the bonding challenge between the thin films and high-temperature flexible polyimide substrates. Through the optimization of fabrication processing and nominal doping concentration of Ce, the thin films show a power factor of $>100 \mu\text{W m}^{-1} \text{K}^{-2}$ and a ZT close to 0.6 at 653 K. After >2000 bending cycle tests at a radius of 4 mm, only a 6 % change in resistivity can be observed. Additionally, the assembled p-type $\text{Fe}_3\text{CoSb}_{12}$ -based flexible device exhibits a power density of $135.7 \mu\text{W cm}^{-2}$ under a temperature difference of 100 K with the hot side at 623 K. This work fills a gap in the realization of flexible thermoelectric devices in the medium-to-high-temperature range and holds significant practical application value.

The increasing demand for wearable electronic devices underscores the need for stable, efficient, and flexible energy solutions to meet their power requirements¹. Compared to traditional batteries², flexible thin-film-based thermoelectric materials and devices exhibit characteristics such as lightweight, bendability, wearability, and simple structure³. They can closely adhere to heat sources, converting temperature differences into electrical energy, serving as power sources and therefore greatly reducing or even eliminating reliance on external power sources⁴. To achieve high energy conversion efficiency, the thin-film materials constituting these devices should possess excellent thermoelectric performance. The figure of merit $ZT = (S^2\sigma/\kappa)T$ of thermoelectric materials is a parameter that measures the performance of the material in the thermoelectric conversion, where $S^2\sigma$ represents the power factor consisting of electrical conductivity σ and the Seebeck coefficient S , κ is the thermal conductivity contributed by

both electrons (κ_e) and lattice (κ_l) components ($\kappa = \kappa_e + \kappa_l$), and T is the absolute temperature (K)⁵. However, optimizing the ZT value of thermoelectric materials has always been challenging due to the close correlation of many physical parameters, including S , σ , and κ_e , with the carrier concentration n ⁶. Till now, band engineering⁷, defect engineering⁸, and other strategies have been commonly employed for structural and compositional control to optimize overall thermoelectric performance⁹.

In addition to requiring excellent thermoelectric performance, high stability and flexibility are also important considerations for practical applications¹⁰. Currently, flexible thermoelectric thin films are mainly divided into three types, namely organic, inorganic, and composite films¹¹. Among them, organic films exhibit advantages such as high flexibility, low cost, low toxicity, and lightweight¹². However, their lower thermoelectric performance, especially the difficulty in

¹State Key Laboratory of Solidification Processing, Northwestern Polytechnical University, Xi'an 710072, P. R. China. ²School of Chemistry and Physics, ARC Research Hub in Zero-emission Power Generation for Carbon Neutrality, and Centre for Materials Science, Queensland University of Technology, Brisbane, Queensland 4000, Australia. ³MOE Key Laboratory of Material Physics and Chemistry Under Extraordinary Conditions, School of Physical Science and Technology, Northwestern Polytechnical University, Xi'an 710072, P. R. China. ⁴These authors contributed equally: Dou Li, Xiao-Lei Shi.

✉ e-mail: zhonghong123@nwpu.edu.cn; lsm@nwpu.edu.cn; zhigang.chen@qut.edu.au

improving the S , hinders their commercialization¹². Also, their poor temperature resistance, which is usually used at <500 K, also limits their application in medium-to-high-temperature environments¹². Although the thermoelectric properties of organic-inorganic composite films have risen to some extent¹⁰, the mechanism behind performance enhancement is complex¹², and their temperature resistance is still limited by the organic matrix¹⁰. Therefore, depositing inorganic materials on flexible substrates is another way of achieving flexible thermoelectric thin films. Among inorganic thermoelectric thin films, Bi_2Te_3 ^{13,14}, as well as silver chalcogenides such as Ag_2Se ^{15,16}, have exhibited excellent near-room-temperature ZT values ($ZT > 1$ at 400 K). However, the reported inorganic flexible thermoelectric thin films are currently limited to functionalities near room temperature¹⁰. This is because with increasing the temperature, the thermoelectric performance of these inorganic flexible films gradually deteriorates in the medium-to-high temperature range (e.g., from 500 K to 700 K)^{15,17}, and Te and Se are prone to volatilize in this temperature range, leading to reduced film stability¹⁸. Considering the enormous application potential and commercial value of flexible thermoelectric materials and devices designed for higher temperatures, especially in nonplanar thermoelectric power generation and refrigeration, there is an urgent need for a new type of flexible film. This film must possess high thermoelectric performance at higher temperatures with outstanding flexibility and stability, which is still a considerable challenge that needs to be tackled.

Compounds with the skutterudite structures have garnered widespread concern for their excellent thermal stability, appropriate S , and enhanced σ ^{19–23}, achieving preliminary success in the preparation of thermoelectric thin-film materials for higher-temperature applications²⁴. In the reported skutterudite thin films, most are currently rigid films due to the long-standing challenge of compatibility between skutterudite and flexible organic substrates. Currently, n-type CoSb_3 -based skutterudite thin films have shown significant progress, with reported $S^2\sigma$ of $210 \mu\text{W m}^{-1} \text{K}^{-2}$ at room temperature²⁵ and ZT of 1.1 at 683 K through rational elemental doping²⁶. However, CoSb_3 -based thin films still face two major challenges, namely realizing highly flexible films (i.e., solving the compatibility issue between skutterudite thin film and high-temperature flexible organic substrates), and achieving high-performance p-type films. For p-type skutterudite thin films, the low σ and S result in less-than-ideal thermoelectric performance, as summarized in Supplementary Table 1^{24,27–37}. Additionally, the brittleness of inorganic skutterudite materials limits their practical application in irregular bending structures. Therefore, developing high-performance p-type flexible skutterudite thin films is of utmost importance.

To address this long-standing challenge, through the guidance of the first-principles calculations and fabrication optimization, we successfully achieve p-type $\text{Fe}_3\text{CoSb}_{12}$ -based skutterudite thin films with exceptional stability, flexibility, and thermoelectric properties in the medium-to-high temperature range. We address the bonding issue between thin films and high-temperature flexible polyimide (PI) by developing self-made target materials and employing advanced pulsed laser deposition (PLD) techniques. By adjusting the nominal doping concentration of Ce, we optimize the hole carrier density, achieving a high $S^2\sigma$ exceeding $100 \mu\text{W m}^{-1} \text{K}^{-2}$, resulting in a ZT value approaching 0.6 at 653 K. Furthermore, our flexible films show outstanding flexibility with only a 6 % change in electrical transport properties after over 2000 bending cycle tests at a radius r of 4 mm, indicating strong adhesion between the film and the high-temperature flexible substrate. Additionally, we introduce, for the first time, a p-type $\text{Fe}_3\text{CoSb}_{12}$ -based flexible device, achieving a power density ω of $135.7 \mu\text{W cm}^{-2}$ at a temperature difference (ΔT) of 100 K with the hot end at 623 K. This groundbreaking work fills a critical gap in the realization of flexible thermoelectric devices in the medium-to-high-temperature range, holding significant practical application value.

Results

To achieve p-type CoSb_3 -based thin films, one should first design the nominal composition. It is well known that Fe has one fewer 3d electron than Co, substituting Fe on Co sites in the $\text{Co}_4\text{Sb}_{12}$ structure can generate one hole in the valence band^{38,39}. Therefore, substituting Fe for Co can induce to formation of p-type skutterudite. However, Fe-doping brings about severe instability in skutterudite phase formation due to charge imbalance^{40–42}. Hence, it is necessary to fill the high charge state filler atoms to neutralize the high hole concentration and achieve electrical neutrality conditions in the p-type skutterudite system. Ce has been proven to be an excellent candidate filler for skutterudite due to its outstanding performance and low cost in bulk materials. Therefore, the synergistic control of Ce-filling and Fe-substitution for Co aims to regulate the p-type thermoelectric performance of the pristine CoSb_3 ^{38,39,42–47}. To validate this concept, first-principles calculations were performed in this work. Figure 1a–c show the calculated band structures of CoSb_3 ($\text{Co}_4\text{Sb}_{12}$), $\text{Fe}_3\text{CoSb}_{12}$, and $\text{CeFe}_3\text{CoSb}_{12}$. It can be observed that pristine CoSb_3 has a low band gap of 0.135 eV, showing a typical semiconducting behavior. By substituting Fe for Co, the Fermi energy level shifts into the valence band, demonstrating its p-type semiconducting properties, albeit with a wider band gap. Further doping with Ce can narrow the band gap and allow for Fermi-level position readjustment. Thus, by adjusting the filling amount of Ce, the comprehensive thermoelectric performance of the p-type $\text{Fe}_3\text{CoSb}_{12}$ skutterudite system can be effectively regulated. It is worth noting that we also calculated the electronic structure of $\text{CeCo}_4\text{Sb}_{12}$ to validate the effect of Ce, as displayed in Supplementary Fig. 1. Ce filling can shift the Fermi level towards the conduction band, thereby demonstrating its ability to adjust the Fermi-level position to optimize the thermoelectric performance of $\text{Fe}_3\text{CoSb}_{12}$.

Moreover, unlike the use of common rigid substrates (such as silicon wafers²⁸, glass³², and quartz³⁵, seen in Supplementary Table 1), all thin film preparation processes need to be re-explored and optimized to address the compatibility issue between skutterudite thin films and high-temperature flexible organic substrates. In this study, we utilized self-designed high-purity targets and employed advanced pulsed laser deposition (PLD) techniques to prepare p-type $\text{Fe}_3\text{CoSb}_{12}$ -based flexible thermoelectric thin films (Supplementary Fig. 2), as detailed in the experimental section of the Supporting Information. Combining p-type skutterudite thermoelectric thin films with high-temperature flexible polyimide (PI) substrates. The essential requirements for the substrate include superior flexibility, insulation, and high-temperature resilience. Polyimide films aptly fulfill these requirements, hence our selection. Detailed information about polyimide film can be seen in Supplementary Fig. 3 and Supplementary Table 2, we fabricated flexible thermoelectric thin films capable of normal operation at high temperatures ($T > 600$ K) and exhibiting high-temperature sensing functionality. We compared the maximum operating temperatures of flexible films, including organic, composite, and inorganic films, as shown in Fig. 1d. Our p-type skutterudite thermoelectric thin films have a maximum operating temperature of 653 K, which is competitively high compared to the reported operating temperatures of other films^{27,48–57}. Furthermore, our films possess high flexibility and stability, with a low normalized resistance R/R_0 (the starting resistance is represented by R_0 , and the resistance after 2000 repeated bending is denoted by R . The bending radius r is 4 mm.), reaching -1.06. Figure 1e compares the flexibility of our films with previously reported films^{13,14,52–54,56,58–67}, demonstrating the excellent flexibility of our p-type skutterudite films. Detailed flexibility data are provided in Supplementary Table 3^{13,14,52–54,56,58–67}. More importantly, our p-type flexible skutterudite film-based device exhibits good output power performance over a broad temperature window, operating from room temperature to even over 600 K (Fig. 1f). The as-assembled device also shows a ω of $135.7 \mu\text{W cm}^{-2}$ at a ΔT of 100 K with the hot-end

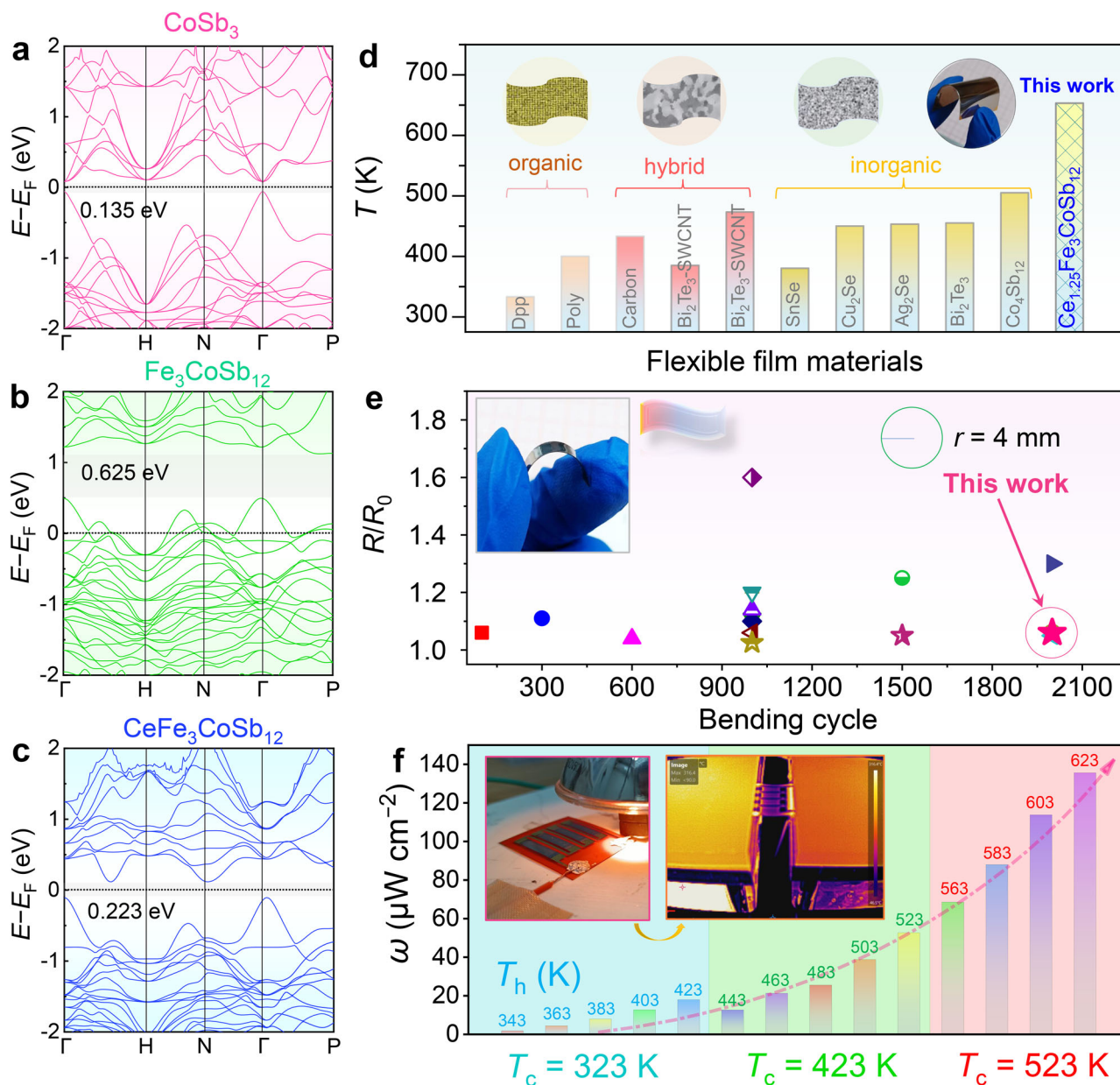


Fig. 1 | Introduction of p-type CoSb_3 -based skutterudite flexible thin films. Calculation of band structures (a) CoSb_3 ($\text{Co}_4\text{Sb}_{12}$), (b) $\text{Fe}_3\text{CoSb}_{12}$, and (c) $\text{CeFe}_3\text{CoSb}_{12}$. (d) Maximum operating temperatures of various flexible thermoelectric thin films^{27,48–57}. The inset schematic diagrams illustrate different types of films, along with a photograph of the p-type Ce-filled $\text{Fe}_3\text{CoSb}_{12}$ flexible thin film reported in this work. (e) Comparison of the normalized resistance R/R_0 (the starting resistance is represented by R_0 , the resistance after 2000 repeated bending is

denoted by R) of the films prepared in this work with those reported^{13,14,52–54,56,58–67}. The minimum bending radius r in this work is 4 mm. The inset photograph illustrates the film reported in this work during bending. (f) Measured power density ω as a function of temperature difference ΔT at different hot-side temperature T_h and cold-side temperature T_c values between the p-type Ce-filled $\text{Fe}_3\text{CoSb}_{12}$ flexible thin-film-based device. The inset image presents the photographs of the thin film flexible generator and testing apparatus.

temperature T_h at 623 K, showing their application prospect for power generation in the medium-to-high temperature range.

Phase and structural characterizations

To optimize the thermoelectric properties of $\text{Fe}_3\text{CoSb}_{12}$ -based flexible thin films, we chose Ce as filling atoms and adjusted the doping concentration of Ce. Experimentally, we deposited five different compositions of $\text{Fe}_3\text{CoSb}_{12}$ -based thin films on high-temperature PI substrates, defined with a nominal composition of $\text{Ce}_x\text{Fe}_3\text{CoSb}_{12}$ ($x = 0.25, 0.50, 0.75, 1.25, \text{ and } 1.50$). To investigate the phase composition and structure of the as-prepared p-type films, we first characterized all film samples using X-ray diffraction (XRD). Figure 2a shows their XRD patterns. The 2θ range is from 20° to 67° . By

comparing with the standard peaks of CoSb_3 (PDF # 47-1769), it can be observed that the main phase of all film samples is CoSb_3 . Particularly, all samples exhibit distinct characteristic peaks such as (310), (321), and (420), demonstrating our successful preparation of CoSb_3 on flexible substrates, which is a significant breakthrough in the field. As the nominal doping content of Ce increases, the peaks of the CoSb_3 phase become more prominent, indicating an increase in the proportion of the CoSb_3 phase in the films. This confirms that the introduction of Ce can stabilize the formation of the CoSb_3 phase. Additionally, through careful comparison, we also found slight traces of impurity phases in the films, such as elemental Sb and FeSb_2 phases. This is a common occurrence during the film deposition process and is challenging to avoid. We will discuss the potential

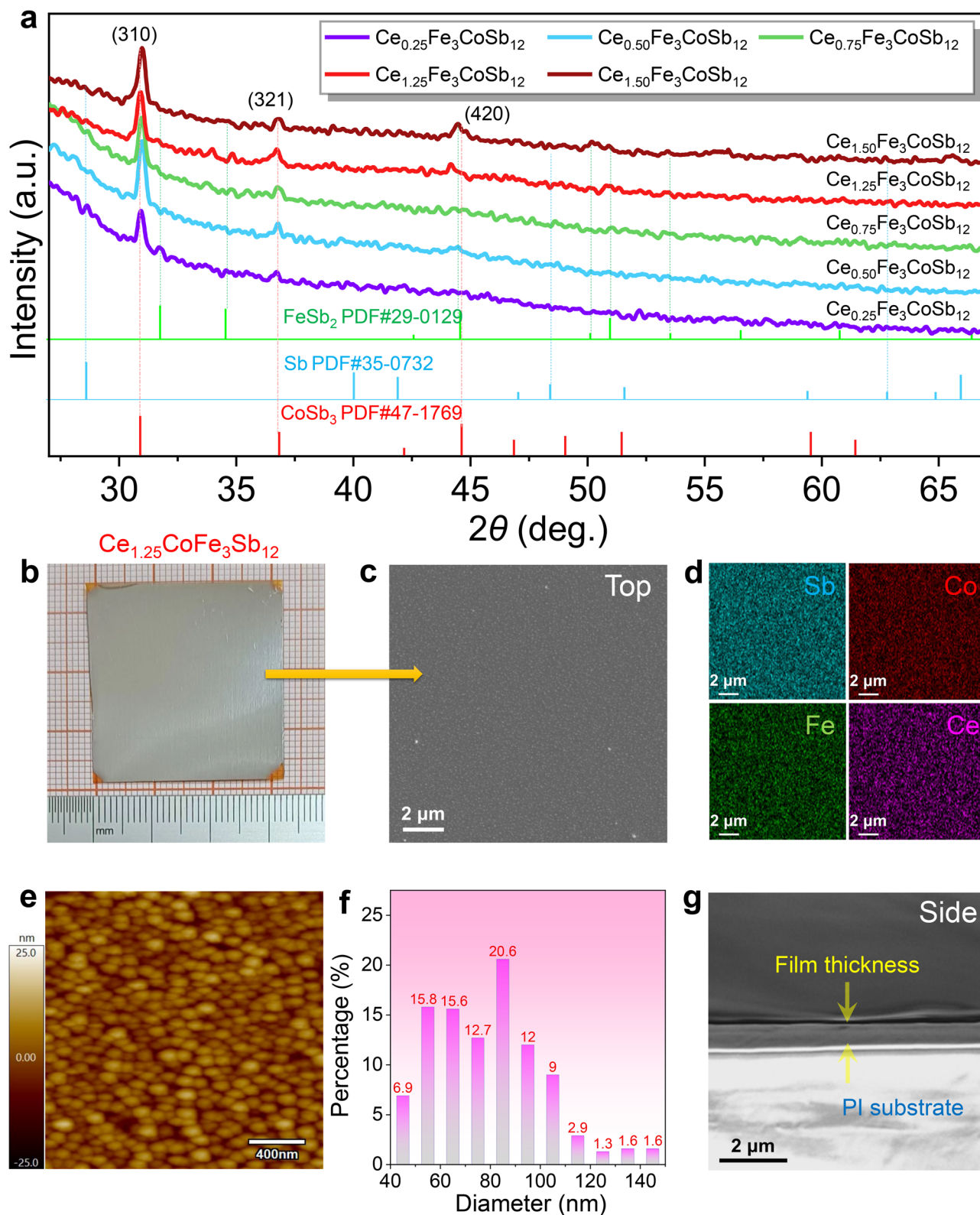


Fig. 2 | Phase and structural characterizations of p-type CoSb_3 -based skutterudite flexible thin films. **a** X-ray diffraction (XRD) patterns of $\text{Ce}_x\text{Fe}_3\text{CoSb}_{12}$ thin films ($x = 0.25, 0.50, 0.75, 1.25,$ and 1.50) on flexible polyimide (PI) substrates. The 2θ range is from 20° to 67° . **b** Photograph of a $\text{Ce}_{1.25}\text{Fe}_3\text{CoSb}_{12}$ flexible thin film on a PI substrate from a top view. The size of the thin film is $>30 \times 30 \text{ nm}^2$. **c** Top-view

scanning electron microscopy (SEM) image of $\text{Ce}_{1.25}\text{Fe}_3\text{CoSb}_{12}$ thin film and **(d)** corresponding energy dispersive spectrometry (EDS) maps for Sb, Co, Fe, and Ce. **e** Atomic force microscopy (AFM) image of $\text{Ce}_{1.25}\text{Fe}_3\text{CoSb}_{12}$ thin film. **f** Percentage distribution of nanoparticle diameters in the film structure. **g** SEM image of a $\text{Ce}_{1.25}\text{Fe}_3\text{CoSb}_{12}$ flexible thin film on a PI substrate from a cross-sectional view.

impact of these impurity phases on the performance of thermoelectric films carefully later.

To comprehensively characterize the morphology of the as-prepared flexible films, we conducted a series of micro/nanostructure characterizations on the film samples. Taking the $\text{Ce}_{1.25}\text{Fe}_3\text{CoSb}_{12}$ film as an example, Fig. 2b displays its optical image, exhibiting a typical metallic luster. The optical images of the PI substrate and the p-type film on the substrate are shown in Supplementary Fig. 4 for reference. Figure 2c presents the scanning electron microscope (SEM) top-view image of the $\text{Ce}_{1.25}\text{Fe}_3\text{CoSb}_{12}$ film, revealing a relatively smooth surface with uniformly distributed small particles, which is a typical characteristic compared to films deposited by other PLD techniques^{68,69}. Supplementary Fig. 5 provides an enlarged SEM image for clearer observation of surface morphology features. Figure 2d presents the corresponding energy-dispersive X-ray spectroscopy (EDS) map of Ce, Sb, Fe, and Co. All elements are distributed uniformly at the micrometer scale, confirming the successful Ce-doping and relatively uniform composition of the as-prepared film without apparent element segregation. SEM and EDS data for $\text{Ce}_x\text{Fe}_3\text{CoSb}_{12}$ films with other Ce filling contents ($x=0.25, 0.50, 0.75,$ and 1.50) can be referenced in Supplementary Figs. 6–9. Figure 2e presents the atomic force microscope (AFM) image of the $\text{Ce}_{1.25}\text{Fe}_3\text{CoSb}_{12}$ film, revealing nanosized particle islands interconnected by atomic stacking, forming a unique nanoparticle structure, where over 80 % of the sizes are below 100 nanometers, as shown in the statistical data in Fig. 2f, sourced from AFM machine testing data. AFM data for $\text{Ce}_x\text{Fe}_3\text{CoSb}_{12}$ films with other Ce doping levels can be referenced in Supplementary Fig. 10. Figure 2g shows the side-view SEM image of the $\text{Ce}_{1.25}\text{Fe}_3\text{CoSb}_{12}$ film, indicating a uniformly thick film with a thickness of approximately 300 nm. Side-view SEM images for all other films are offered in Supplementary Fig. 11 as a reference. All this evidence confirms the successful growth of $\text{Ce}_x\text{Fe}_3\text{CoSb}_{12}$ films on flexible PI substrates.

Compositional characterizations

Although the evidence from SEM-EDS indicates uniformity of all elements at the microscale, considering the typical granular morphology of the film, further investigation into the nanoscale elemental distribution is necessary. For this purpose, we employed transmission electron microscopy (TEM)-EDS to characterize the composition of localized regions of the film in detail. The TEM samples were prepared using a combination of manual peeling and alcohol sonication techniques. Figure 3a presents the TEM high-angle annular dark-field (HAADF) image of a flexible film with a nominal composition of $\text{Ce}_{1.25}\text{Fe}_3\text{CoSb}_{12}$, and the corresponding EDS maps of each element are shown in Fig. 3b (the overlap map of all elements can be seen in Supplementary Fig. 12). Here, Ce and Sb are predominantly distributed within the nanoparticles, while Co and Fe are more concentrated at the boundaries of the nanoparticles, displaying significant compositional fluctuations. However, it is important to note that these compositional fluctuations may also arise from variations in surface morphology due to non-planar surfaces. Figure 3c provides a statistical analysis of the actual compositions of Ce, Co, Fe, and Sb at 14 points in Fig. 3a. More detailed composition information is available in Supplementary Figs. 13–27 and Supplementary Table 4. The atomic percentage of the dopant element Ce fluctuates between 0.88 % and 1.98 %, remaining relatively stable overall, with an average atomic percentage exceeding 1 %, indicating successful doping. The atomic percentages of Fe and Co exhibit opposite trends, with their sum remaining essentially constant, consistent with the design principles of the nominal composition. Additionally, a comparison of the atomic percentages of Ce and Fe at different locations is presented in a line graph in Fig. 3d, illustrating the fluctuations caused by compositional variations. These rational fluctuations in composition within the nanoscale regions do not hinder the formation of the skutterudite phase, but aid in scattering phonons,

thereby potentially reducing κ . Figure 3e shows the nominal compositions of different elements in $\text{Ce}_x\text{Fe}_3\text{CoSb}_{12}$ thin films ($x=0.25, 0.50, 0.75, 1.25,$ and 1.50), while Fig. 3f presents the actual compositions of different films as determined by EDS. More detailed composition information is available in Supplementary Table 5. Significant differences between nominal and actual compositions are observed, particularly in the substitution ratio of Fe atoms for Co atoms compared to the nominal composition. However, the Fe content is sufficient to modulate pristine $\text{Co}_4\text{Sb}_{12}$ films into p-type semiconductors, achieving the desired composition. The addition of Ce is aimed at providing sufficient electrons to neutralize excess holes in the $\text{Fe}_3\text{CoSb}_{12}$ system, thereby stabilizing the formation of the p-type skutterudite phase. Hence, it is understandable for the actual doping level of Ce to be lower than its nominal concentration when the Fe content in the actual composition is lower than the nominal composition. Figure 3g compares the actual and nominal doping levels of Ce in different films, providing a more intuitive representation of their variations and differences. We predict that the actual content of Ce will play a decisive part in the thermoelectric properties of the flexible skutterudite film. Besides, we also studied the elemental composition distribution in different regions of the $\text{Ce}_{1.25}\text{Fe}_3\text{CoSb}_{12}$ film (Supplementary Figs. 28–30) and found that the distribution characteristics of elements in different regions were consistent, demonstrating the macroscopic homogeneity of the film.

Nanostructural characterizations

In addition to compositional information, we carefully studied the nanostructure of the as-deposited films to fully understand their structural characteristics. Figure 4a presents a typical low-magnification TEM image of the $\text{Ce}_{1.25}\text{Fe}_3\text{CoSb}_{12}$ flexible film. As can be seen, the film is composed of numerous typical island-like large grains with sizes around 60 nanometers and small grains of only a few nanometers between these large grains. Figure 4b displays the corresponding selected area electron diffraction (SAED) pattern, indicating typical nano-polycrystalline features. Figure 4c displays a high-resolution TEM (HRTEM) image of one of the island-like large grains, revealing single-crystalline characteristics without apparent internal interfaces within the grain. Also, the Moiré fringes at the interfaces between this grain and others, further demonstrate the single-crystalline nature of these grains. Figure 4d depicts the HRTEM image of the small grains taken from Fig. 4a, showing clear interfaces between these small grains with different orientations, indicating the polycrystalline nanocrystalline characteristics. Figure 4e shows an HRTEM image of the small grains after tilting the zone axis, displaying the film potentially tilted to the [001] direction, which is verified via the initially indexed results. Figure 4f presents a corresponding filtered HRTEM image, confirming the potential presence of many lattice defects, such as lattice distortions and edge-like dislocations. These lattice defects combined with dense grain boundaries contribute positively to the reduction of κ in the film. Regarding the inclusion phase, Fig. 4g displays an HRTEM image of another large grain, and the corresponding fast Fourier transform (FFT) pattern is shown as an inset image, suggesting overlapping FFT patterns. Unlike Fig. 4c, different nanoregions with different orientations coexist within this grain. Figure 4h shows a magnified HRTEM image taken from Fig. 4g, revealing relatively evenly distributed dense nanoinclusions with similar sizes of approximately 5 nm, close to quantum size. Such quantum-sized inclusions potentially contribute to the reduction of κ in the film⁹. Figure 4i displays the corresponding filtered HRTEM image to highlight significant differences in lattice between the quantum-sized inclusions and matrix. Although we cannot directly prove the composition of these inclusion phases at such a small-scale area, all the above evidence is sufficient to illustrate the specific nanostructure features of the as-fabricated flexible films.

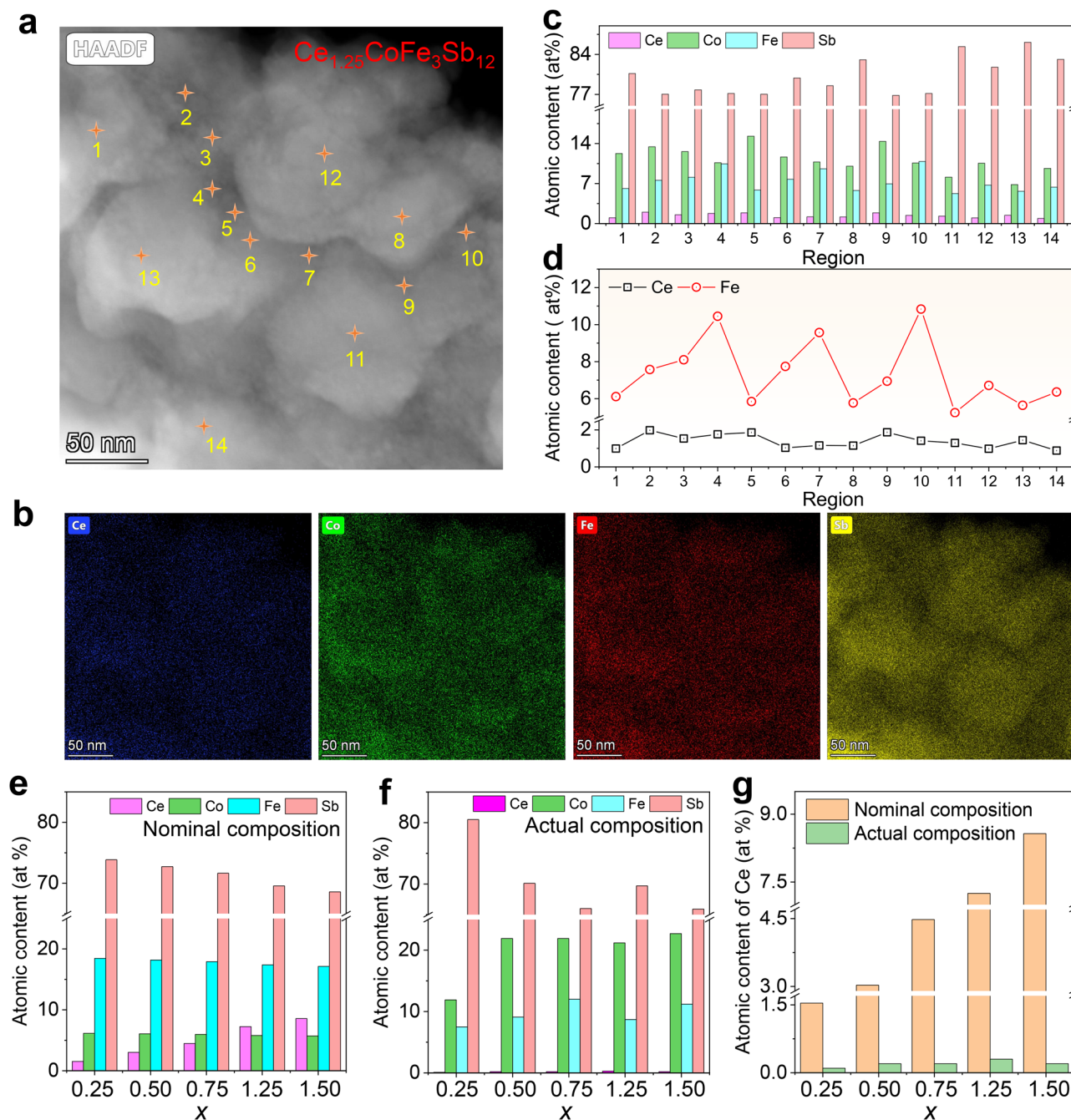


Fig. 3 | Compositional characterizations of p-type $\text{Ce}_{1.25}\text{Fe}_3\text{CoSb}_{12}$ flexible thin film. **a** Transmission electron microscopy (TEM) high-angle annular dark-field (HAADF) image of the $\text{Ce}_{1.25}\text{Fe}_3\text{CoSb}_{12}$ thin film used for compositional analysis, featuring 14 EDS points, and **(b)** corresponding EDS maps of Ce, Co, Fe, and Sb. **c** Atomic contents of different elements (Ce, Co, Fe, and Sb) obtained within

different EDS spot regions in **(a)**. **d** Variations of atomic contents of Ce and Fe elements obtained within different EDS spot regions in **(a)**. **e** Nominal and **(f)** actual atomic contents of $\text{Ce}_x\text{Fe}_3\text{CoSb}_{12}$ thin films ($x = 0.25, 0.50, 0.75, 1.25$, and 1.50) for Ce, Co, Fe, and Sb. **g** Comparison of nominal and actual atomic contents of $\text{Ce}_x\text{Fe}_3\text{CoSb}_{12}$ thin films ($x = 0.25, 0.50, 0.75, 1.25$, and 1.50) for Ce.

Thermoelectric performance

We conducted a thorough study on the thermoelectric properties of flexible films. Figure 5a–c illustrate the temperature-dependent σ , S , and $S^2\sigma$ of $\text{Ce}_x\text{Fe}_3\text{CoSb}_{12}$ ($x = 0.25, 0.50, 0.75, 1.25$, and 1.50) thin films. As we can see, the σ of all p-type films initially rises with temperature increasing, showing typical semiconductor behavior; moreover, the positive S value indicates that the films are all p-type films. Additionally, $|S|$ decreases at high temperatures due to bipolar diffusion effects^{70–72}. Finally, we achieve a high $S^2\sigma$ of $>100 \mu\text{W m}^{-1} \text{K}^{-2}$ at 653 K when $x = 1.25$. The variations in the electrical transport properties of the flexible thin-film samples are not significantly related to the changes in nominal

composition. Conversely, the changes in thermoelectric properties are strongly linked to the variations in the actual composition of the flexible films (see Fig. 3f, g and Supplementary Table 5). Specifically, when the actual doping level of Ce is higher, the film exhibits significantly higher σ and $S^2\sigma$. Additionally, due to the presence of some nano-inclusion phases within the film, such as elemental Sb and FeSb_2 compound (unit cells can be referred to Supplementary Figs. 31, 32), as shown by XRD and TEM results, the impact of these inclusion phases on the overall thermoelectric properties of the thin films cannot be ignored, which may lead to the considerable complexity of the electrical transport properties. We conducted first-principles calculations to determine the

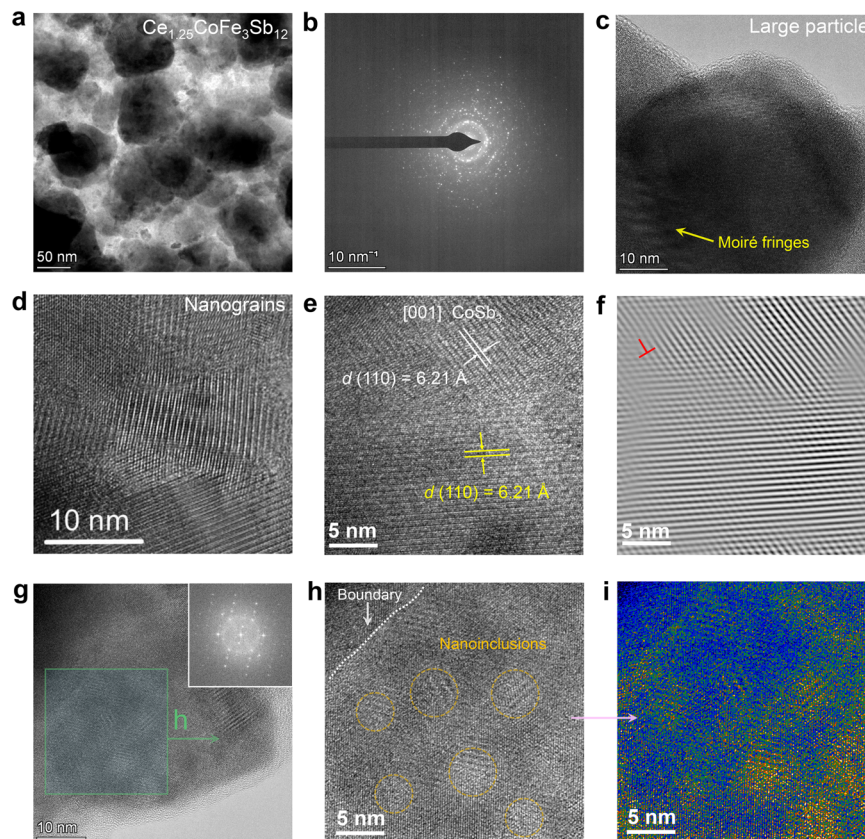


Fig. 4 | Nanostructural characterizations of $\text{Ce}_{1.25}\text{Fe}_3\text{CoSb}_{12}$ flexible thin film. **a** Low-magnification TEM image of the $\text{Ce}_{1.25}\text{Fe}_3\text{CoSb}_{12}$ thin film used for nanostructure analysis. **b** Corresponding selected area electron diffraction (SAED) pattern. **c** TEM image of a large particle in the thin film structure. **d** High-resolution TEM (HRTEM) image of nanograins between large particles. **e** HRTEM image of nanograins taken from another area with indexed lattice information.

f Corresponding filtered HRTEM image to show lattice distortions and a potential edge-like dislocation. **g** TEM image of a large particle with quantum-dot-sized nano-inclusions in it. The inset shows a corresponding fast Fourier transform (FFT) pattern. **h** HRTEM image of these quantum-dot-sized nano-inclusions magnified from (g). **i** Corresponding filtered image.

electronic structures of elemental Sb and FeSb_2 compounds (Supplementary Figs. 33, 34). The results show that elemental Sb exhibits typical semi-metallic characteristics with overlapping conduction and valence bands, which may release free electrons to neutralize the hole carrier concentration, while the FeSb_2 compound is a typical semiconductor, hence its mechanism of affecting the overall performance is more complex. To understand the changes in the electrical transport properties of the thin films, Fig. 5d displays the room-temperature carrier concentration n and mobility μ as a function of x . Generally, higher Ce content in the actual composition leads to lower n , confirming that the addition of Ce can indeed optimize the hole carrier concentration, reflecting the rationality of our initial design concept. Moreover, the μ of all film samples is considerably low due to the presence of numerous defects within the film, as mentioned earlier, which may scatter carriers during their transportation, leading to a significant decrease in μ and in turn σ . Especially when x is 1.50, the insufficient doping of Ce in the actual composition combined with the excessive doping of Ce in the nominal composition increases the structural complexity, leading to lower μ . The room-temperature effective mass m^* is shown in Fig. 5e, as a function of x calculated through a single parabolic band (SPB) model. Essentially, as the nominal Ce doping level increases, the m^* gradually decreases, indicating the annihilation of free electrons released by the Ce doping of hole carriers. Figure 5f displays the estimated temperature-dependent ZT of $\text{Ce}_{1.25}\text{Fe}_3\text{CoSb}_{12}$ flexible thin film based on its measured room-temperature κ . The inset shows the sample for κ measurement. We used commercial equipment to test the thermal diffusivity D of the film (equipment photos and testing principles can be found in Supplementary Fig. 35) and roughly calculated the κ of the film

using the measured density and specific heat capacity C_p of the target materials, with a room temperature κ of only $0.113 \text{ W m}^{-1} \text{ K}^{-1}$. Due to the presence of numerous lattice defects within the film, as mentioned earlier, which may scatter phonons effectively of almost every wavelength, the low κ is understandable. The presence of grains within 100 nanometers in flexible skutterudite films is more than 80%, effectively scattering phonons. Considering that the mean free path of phonons in CoSb_3 is reported around $80 \text{ nm}^{73,74}$, this scattering mechanism is pivotal in reducing thermal conductivity. It should be noted that testing temperature-dependent D is challenging for flexible thin-film materials, so we only used the room temperature κ to estimate ZT at variable temperatures, obtaining a value as high as 0.6 at 653 K. Since there are very few reports about the thermoelectric properties of flexible p-type CoSb_3 thin films, the data we obtained is still meaningful. When determining the κ , we use the density of target materials rather than that of the thin films due to the difficulty in directly measuring the thin film density. Considering the actual granular structure of the thin film, it should result in a lower actual thin film density than the target density, therefore the actual ZT of the thin film is likely to be even higher.

Flexibility and high-temperature sensing

Figure 6a displays photos taken before and during the bending process of $\text{Ce}_{1.25}\text{Fe}_3\text{CoSb}_{12}$ film using our self-designed automatic repeat bending film instrument and Owon BT35+ multimeter (Supplementary Movies 1, 2), demonstrating the excellent flexibility of the film. Figure 6b shows the relationship between R/R_0 and r of the $\text{Ce}_{1.25}\text{Fe}_3\text{CoSb}_{12}$ film after 1000 bending cycles. Generally, higher R/R_0 usually results in a higher degree of film bending¹⁴. However, the

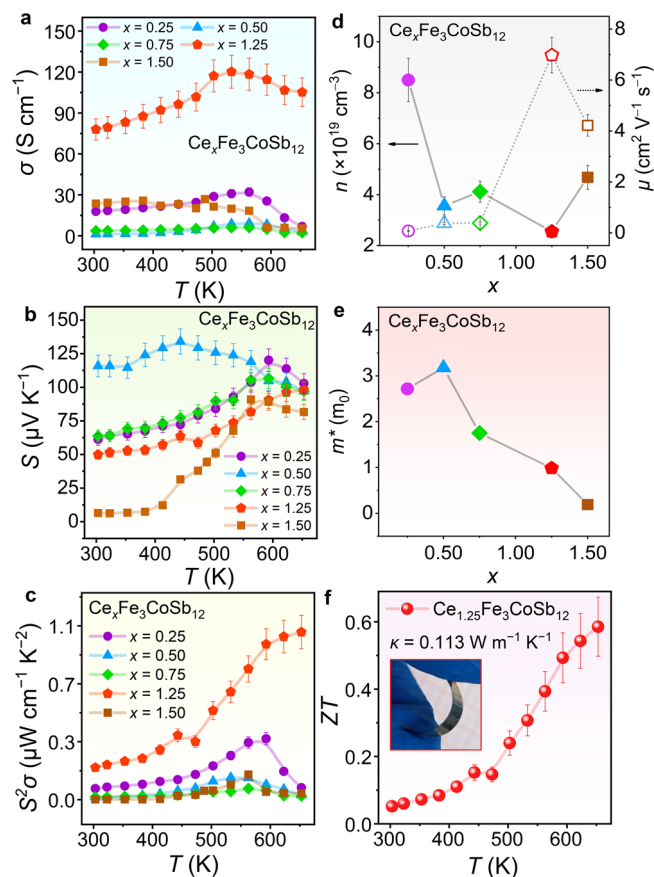


Fig. 5 | Thermoelectric performance of p-type CoSb_3 -based skutterudite flexible thin films. Temperature-dependent (a) electrical conductivity σ , (b) Seebeck coefficient S , and (c) power factor $S^2\sigma$ of $\text{Ce}_x\text{Fe}_3\text{CoSb}_{12}$ flexible thin films ($x=0.25, 0.50, 0.75, 1.25$, and 1.50). **d** Room-temperature carrier concentration n and mobility μ as a function of x . **e** Room-temperature effective mass m^* as a function of x calculated through a single parabolic band (SPB) model. **f** Estimated temperature-dependent ZT of $\text{Ce}_{1.25}\text{Fe}_3\text{CoSb}_{12}$ flexible thin film based on its measured room-temperature thermal conductivity κ . The inset image displays the film sample for the κ test.

achieved R/R_0 is as low as 1.05 even when r equals 4 mm, proving the high flexibility and stability. Figure 6c depicts the R/R_0 of the $\text{Ce}_{1.25}\text{Fe}_3\text{CoSb}_{12}$ film as a function of the bending cycles, with r maintained at 4 mm. It can be observed that even after 2000 repeated bending, a low R/R_0 of approximately 1.06 can still be achieved, demonstrating extraordinary flexibility and durability. Additionally, for reference, Supplementary Fig. 36 displays photos of film bending under different r values. The excellent flexibility of the films can be attributed to their structure: the films have uniformly dense nano-sized grains with good crystallinity. Through the optimization of deposition, the film thickness was controlled to be thin, approximately 300 nm thick, while the selected flexible substrate is only 125 μm thick. The strong bond between the film and the flexible substrate also enhances flexibility. Figure 6d displays a photo of the self-built light-thermal detection platform. By adjusting the power of the DC power supply, the temperature of the lamp can be controlled. Based on the Seebeck effect, the light spot converges on one side of the flexible thermoelectric film to generate detection signals. More detailed information about the detection platform is shown in Supplementary Fig. 37 for reference. Figure 6e shows the amplified image of the light-thermal detection process. Additionally, an infrared thermal imager captures the temperature distribution on the flexible thermoelectric film during the light-thermal detection

process, as shown in Fig. 6f. It can be observed that there is a significant temperature difference distribution on both sides of the flexible film. The current signal variation over time during the detection process can be obtained by turning the lamp on and off. Figure 6g shows the relationship between the measured current I and the time the focused light beam strikes the flexible thermoelectric film. When the hot side of the thermoelectric film is irradiated by thermal light, current is generated through the thermoelectric film, while the other side remains at ambient room temperature (25 $^\circ\text{C}$). The response speed is considerably fast. As the temperature increases, the detected I gradually increases. When the center temperature of the light spot is 473 K, 523 K, and 643 K, the peak I is 1.8 μA , 2 μA , and 3 μA , respectively. Furthermore, the variation of the I during the detection process under different hot-side temperatures ranging from ambient room temperature (25 $^\circ\text{C}$) to medium-high temperatures is shown in Supplementary Fig. 38 for reference (Supplementary Movie 3 demonstrates detailed information about the platform components, while Supplementary Movies 4, 5 show measurement results). Figure 6h shows the variation of the detected I and voltage V signals with temperature from 300 K to 675 K. This significantly expands the detection temperature range of flexible thermoelectric films and is of great significance for future practical applications, serving as high-temperature flexible sensors. The excellent detection performance is attributed to the good thermoelectric properties of the flexible thermoelectric film as discussed above. The flexible skutterudite thermoelectric film enables thermoelectric detection across a broad temperature spectrum, from room temperature to medium-to-high levels. Its outstanding features, including high-temperature resistance, flexibility, and lightweight nature, make it suitable for applications in environments with complex shapes, particularly in medium and high-temperature settings. Fire-resistant clothing plays a crucial role in safeguarding firefighters during firefighting endeavors. Leveraging the flexible thermoelectric film, a self-powered intelligent fire alarm system can be developed. This system can preemptively alert firefighters before their attire is compromised by fire, allowing them to take timely preventive measures to avoid burns^{75,76}. Utilizing thermoelectric film to enable precise temperature sensing and responsive fire alarm capabilities in combustible materials holds significant importance for establishing a safe home environment^{77,78}. Moreover, a basic thermoelectric hydrogen sensor can be created by applying a catalyst to one side of the thermoelectric film. When exposed to a hydrogen-containing environment, the catalyst facilitates the reaction between hydrogen and oxygen, producing water vapor and releasing heat. Consequently, the end with the catalytic metal deposit becomes hot, while the end without it remains cooler. This temperature gradient generates an electrical signal through the Seebeck effect, enabling the detection of hydrogen concentration.

Fabrication and performance evaluation of generator

To validate the practical application potential of the prepared flexible thermoelectric thin film, we, for the first time, fabricated four-leg $\text{Ce}_{1.25}\text{Fe}_3\text{CoSb}_{12}$ thin-film-based flexible thermoelectric devices and systematically discussed their output performance. The construction process of the thin-film-based device is illustrated in Supplementary Fig. 39 for reference. Figure 7a displays the structure of the as-designed device, where four $\text{Ce}_{1.25}\text{Fe}_3\text{CoSb}_{12}$ thin films are combined via Au electrodes and wires using the traditional four-wire method on a flexible PI substrate. Figure 7b displays the self-built testing platform used to measure the output performance of our designed flexible device (Supplementary Fig. 40 provides detailed information on each part of the platform, and Supplementary Movie 6 demonstrates the measurement process of the device). Figure 7c shows the temperature distribution on the device captured by an infrared camera during the measurement process. It can be observed that there is a significant

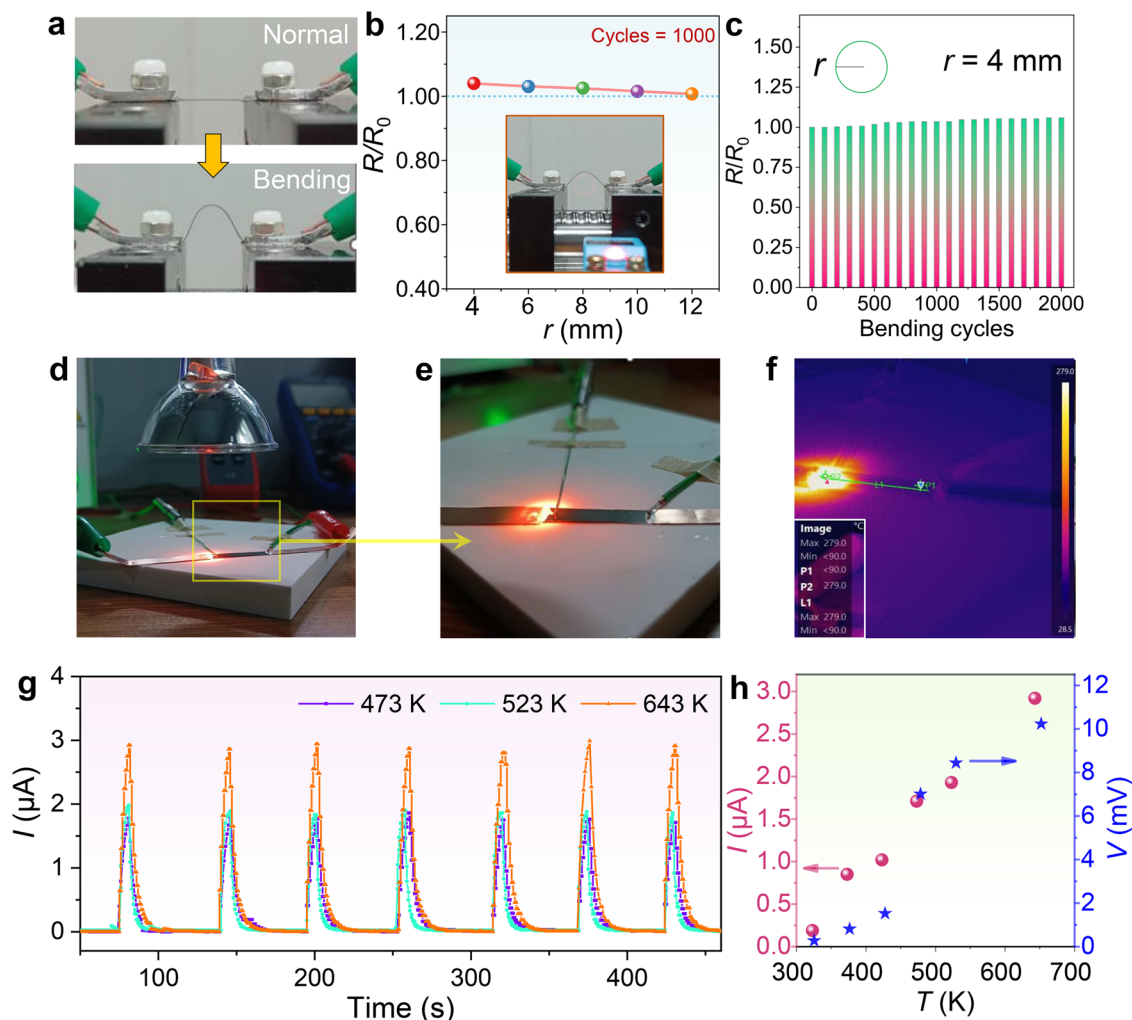


Fig. 6 | Flexibility and high-temperature sensing potential of p-type $\text{Ce}_{1.25}\text{Fe}_3\text{CoSb}_{12}$ flexible thin film. **a** Photographs of the $\text{Ce}_{1.25}\text{Fe}_3\text{CoSb}_{12}$ flexible thin film before and during bending. **b** The relationship between R/R_0 and r after 1000 bending cycles. **c** R/R_0 as a function of bending cycles. Here r is 4 mm. **d** Photograph of the platform used to evaluate the sensing characteristics of the

thin film. **e** Photograph of the setup for illumination testing. The light beam focuses on the side of the thin film and generates a temperature gradient. **f** Temperature distribution on the thin film under infrared imaging. **g** Measured I as a function of time when low frequency is introduced for optical pulse modulation. **h** I and voltage V values at different light temperatures.

temperature difference distribution on both the hot and cold sides of the flexible film device. Change in temperature differences (ΔT) can be obtained by keeping one side of the heating plate at a specified temperature and the other side at another specified temperature, with the hot-side temperature T_h ranging from 563 to 623 K, and the cold-side temperature T_c maintained at 523 K. Supplementary Fig. 41 displays additional temperature difference distributions. Figure 7d shows the experimentally measured open-circuit voltage V_{oc} as a function of ΔT . As ΔT increases from 40 K to 100 K, the V_{oc} increases from 26.7 mV to 37.5 mV. Figure 7e, f show the relationships between the V_{oc} and the output power P as functions of the load current I_{load} measured at different ΔT s, where the P values are 12.3, 15.8, 20.4, and 24.4 nW at ΔT s of 40, 60, 80, and 100 K, respectively. Additionally, it is noteworthy that power density ω is one of the most valuable indexes for evaluating the performance of thermoelectric devices. Figure 7g illustrates the relationship between ω and ΔT . The ω monotonically increases with increasing the ΔT , reaching 68.6, 88.0, 113.7, and 135.6 $\mu\text{W cm}^{-2}$ at ΔT s of 40, 60, 80, and 100 K, respectively. Additionally, we conducted similar measurements by setting the T_c to 323 and 423 K, as shown in Supplementary Figs. 42, 43. Our flexible thin-film-based device exhibits better performance at high temperatures due to the higher thermoelectric properties of the thin films, which can also

be confirmed via Supplementary Figs. 44, 45. Figure 7h illustrates the operation of the $\text{Ce}_{1.25}\text{Fe}_3\text{CoSb}_{12}$ flexible thin-film-based device in harnessing waste heat for power generation under a curved high-temperature surface scenario. The flexible thin-film device was securely affixed to the surface of the high-temperature furnace tube and consistently produced a relatively stable current close to 0.6 μA and voltage near 15 mV, as depicted in Fig. 7i. The temperature of the high-temperature side of the flexible device exceeds 600 K, as evidenced by the infrared image showing the temperature distribution inserted in Fig. 7i. For clearer insights, Supplementary Fig. 46 and Supplementary Movie 7 provide detailed views of the inset pictures. This is the first successful fabrication of p-type flexible CoSb_3 -based film devices, achieving excellent performance over such a wide temperature range from medium to high temperatures, indicating that our designed CoSb_3 -based flexible thermoelectric devices are particularly effective for medium-to-high-temperature scenarios, filling the gap in high-temperature flexible thermoelectric power generation.

In this study, a p-type CoSb_3 -based skutterudite flexible thin films, nominally composed of $\text{Ce}_{1.25}\text{Fe}_3\text{CoSb}_{12}$ with an enhanced $S^2\sigma$ of $>100 \mu\text{W m}^{-1} \text{K}^{-2}$ and an approximated ZT of ~ 0.6 at 653 K, has been fabricated using an advanced PLD technique with a self-designed

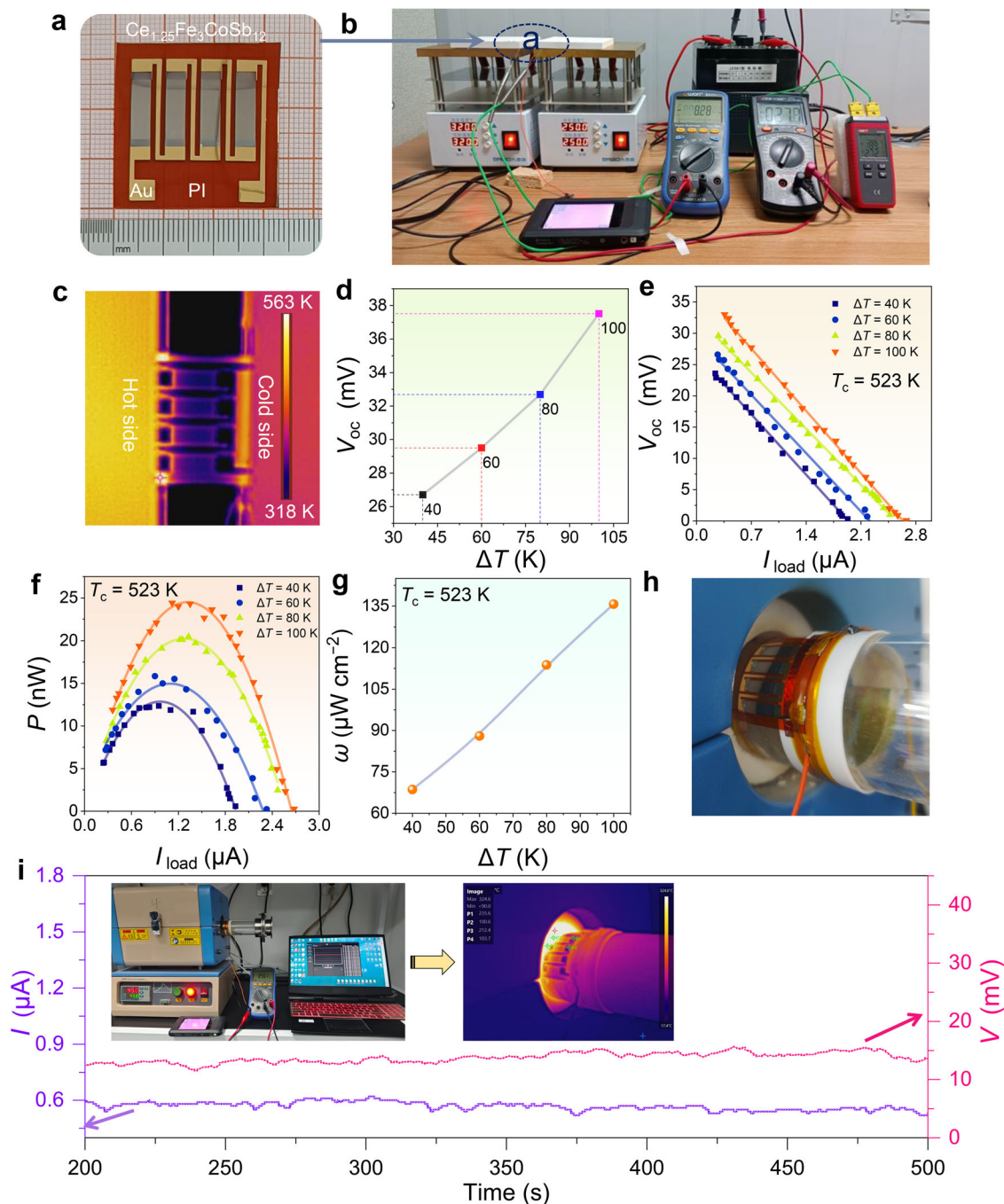


Fig. 7 | Fabrication and performance evaluation of p-type $\text{Ce}_{1.25}\text{Fe}_3\text{CoSb}_{12}$ thin-film-based flexible thermoelectric generator. **a** Photograph exhibiting the flexible $\text{Ce}_{1.25}\text{Fe}_3\text{CoSb}_{12}$ thin-film-based flexible generator. **b** Photograph exhibiting the testing platform used to assess the performance of the manufactured flexible thin film generator. **c** Infrared photograph of temperature distribution on the flexible device after applying a temperature difference ΔT . **d** The open-circuit voltage V_{oc} of the test varies with ΔT . The cold-side temperature T_c is 523 K. **(e)** V_{oc} and **(f)** output power P of the test vary with load current I_{load} at different ΔT s. The T_c is

523 K. **g** The measurement output power density ω varies with ΔT . Here the T_c is 523 K. **h** Image of the $\text{Ce}_{1.25}\text{Fe}_3\text{CoSb}_{12}$ flexible thin-film-based device securely adhered to the surface of a heating tube furnace. **i** Measurement of I and V over time as the device gathers residual heat from the curved surface of the tube furnace for power generation. An inset displays the photograph of the platform utilized for measuring I and V during waste heat power generation. Another inset presents an infrared image illustrating the surface temperature distribution of the flexible thin-film-based device during waste heat power generation.

target material, resulting in distinctive compacted polycrystalline nanostructures. Leveraging the compact nanostructures and thin, flexible PI substrates, we achieve a low R/R_0 of -1.06 after 2000 repeated bending under a minimum r of only 4 mm, showing unprecedented flexibility. Moreover, we, for the first time, fabricate a p-type $\text{Ce}_{1.25}\text{Fe}_3\text{CoSb}_{12}$ thin-film-based flexible generator, demonstrating a high ω of $135.7 \mu\text{W cm}^{-2}$ at a ΔT of 100 K and a T_c of 523 K. This study fills the gap of high-temperature flexible thermoelectric power generation

and provides insights for designing other high-temperature flexible thermoelectric thin films for practical applications.

Methods

Materials

Sb (purity 99.995%, diameter: 1–10 mm) was purchased from CNBM (Chengdu) Optoelectronic Materials Co., Ltd. Co (purity 99.95%, diameter: 3–10 mm) was purchased from Beijing Gold Crown for The New

Material Technology Co., Ltd. Fe (purity 99.95%, diameter: 3–10 mm) was purchased from Beijing Gold Crown for The New Material Technology Co., Ltd. Ce (purity 99.95%, diameter: 1–10 mm) was purchased from ZhongNuo Advanced Material (Beijing) Technology Co., Ltd. PI substrate was purchased from Shenzhen Runsea Electronic Co., Ltd.

Fabrication of p-type CoSb₃-based flexible thin films

Thin films of Ce_xFe₃CoSb₁₂ ($x = 0.25, 0.50, 0.75, 1.25, \text{ and } 1.50$) were deposited onto flexible PI substrates capable of withstanding temperatures up to 400 °C (673 K). The deposition process utilized a PLD system (Neocera 120) with self-made targets. For instance, a high-purity (99.98%) Ce-doped Fe₃CoSb₁₂ target was obtained via the temperature gradient zone melting (TGZM) route^{26,70,72,79,80}. PI substrates with sizes of 33 mm × 33 mm × 0.125 mm underwent ultrasonic cleaning for 20 min in acetone, 10 min in absolute ethyl alcohol, and 10 min in deionized water, followed by drying in an oven. The PLD chamber was evacuated to a base pressure of 1.5×10^{-4} Pa. Targets were positioned in a holder within the chamber and traversed for uniform ablation of the target surface, ensuring uniform film growth. The distance between the target and the substrate was approximately 10 cm. Substrates were heated using the built-in heater within a range of 20–800 °C. Heating occurred from room temperature to 523 K at a rate of 10 K min⁻¹ and maintained during deposition. The pulsed laser employed was a krypton fluoride excimer laser operating at a 10 Hz repetition rate, 20 ns pulse duration, 248 nm wavelength, and a laser power of 190 ± 5 mJ per pulse. Subsequently, annealing took place for 35 min in an Ar ambient. The temperature increased at a rate of 10 K min⁻¹, with the annealing temperature set at 250 °C, followed by natural cooling to room temperature.

Assembly of CoSb₃ thin-film-based flexible thermoelectric devices

To begin, the electrode mask was placed onto a clean and dry flexible PI substrate and securely fastened using high-temperature tape. Subsequently, a layer of Au electrode, approximately 200 nm thick, was deposited within a vacuum chamber. Following this step, the mask plate was removed, and the substrate was covered with a thin-film thermoelectric arm mask plate, which was also affixed using high-temperature tape and inserted into the vacuum chamber. CoSb₃-based thermoelectric targets were then deposited onto the substrate using PLD. Finally, the film-electrode integrated thermoelectric device was extracted and transferred to a tube furnace for annealing under continuous argon gas protection.

Characterizations

The morphology of the as-grown thin films was examined using field emission SEM (FESEM, Tescan Lyra-3) equipped with EDS operating at 20 kV. Crystalline phases were identified via grazing incidence XRD (GIXRD, XRD-7000S/L) at 2 ° with a 2θ angle range of 20–67 ° and a scanning velocity of 3° min⁻¹, utilizing Cu K α radiation ($\lambda = 0.15406$ nm). The nanostructure was investigated using a TEM (Talos F200x). The temperature distributions of thin films and devices were acquired using a high-performance compact thermal imaging camera for professionals (HM-TPK20-3AQF/W, HIKMICRO Pocket2). AFM (Dimension Icon, Bruker) was utilized to examine the surface morphology in tapping mode. The tapping mode was employed to perform nanoscale topographic characterization of the thin film surface. The tip curvature radius is 35 nm with the type of NSGO3/Au.

Performance evaluation of thin films

The S and σ of the films were concurrently measured using an MRS-3 thin-film thermoelectric test system (Wuhan Joule Yacht Science & Technology Co., Ltd., China). The Hall coefficient R_H was determined using the electrical transport properties measurement system (ET9105-HS, East Changing Technologies, Inc.) at room temperature.

The signified D data of thin films on a substrate were measured using an AC method thermal diffusivity measurement system (Laser PIT, ADVANCE RIKO) under vacuum conditions, with dimensions of 18.05 mm × 8.75 mm × 300 nm. The C_p data were calculated using the SPB model⁸¹, while the mass density d data were obtained from the d of the target materials via the Archimedes method⁸².

Sensing potential evaluation of thin films

For the heat signal response test, light and heat were provided by a halogen tungsten lamp (24 V, 150 W) utilized to drive the lamp. Current I as a function of time was recorded using a Digital Multimeter with Bluetooth (Owon BT35+).

Performance evaluation of thermoelectric generators

The power generation performance of the 4-leg thermoelectric device was monitored using a Digital Multimeter with Bluetooth (Owon BT35+) employing the 4-wire method. The ΔT was regulated using laboratory-made equipment, which controlled the T_h and T_c , along with a variable resistor to adjust the device resistances to maximize the output power.

Data availability

The data generated in this study are provided in the Source Data file. Source data are provided with this paper.

References

1. Yang, Q. et al. Flexible thermoelectrics based on ductile semi-conductors. *Science* **377**, 854–858 (2022).
2. Sun, Y. et al. Biomass-derived carbon for high-performance batteries: from structure to properties. *Adv. Funct. Mater.* **32**, 2201584 (2022).
3. Liu, R., Wang, Z. L., Fukuda, K. & Someya, T. Flexible self-charging power sources. *Nat. Rev. Mater.* **7**, 870–886 (2022).
4. Jia, Y. et al. Wearable thermoelectric materials and devices for self-powered electronic systems. *Adv. Mater.* **33**, 2102990 (2021).
5. Xiao, Y. & Zhao, L.-D. Seeking new, highly effective thermoelectrics. *Science* **367**, 1196 (2020).
6. Zheng, Y. et al. Defect engineering in thermoelectric materials: what have we learned? *Chem. Soc. Rev.* **50**, 9022–9054 (2021).
7. Pei, Y., Wang, H. & Snyder, G. J. Band engineering of thermoelectric materials. *Adv. Mater.* **24**, 6125–6135 (2012).
8. Zhao, C., Li, Z., Fan, T., Xiao, C. & Xie, Y. Defects engineering with multiple dimensions in thermoelectric materials. *Research* **2020**, 9652749 (2020).
9. Shi, X.-L., Zou, J. & Chen, Z.-G. Advanced thermoelectric design: from materials and structures to devices. *Chem. Rev.* **120**, 7399–7515 (2020).
10. Cao, T., Shi, X.-L. & Chen, Z.-G. Advances in the design and assembly of flexible thermoelectric device. *Prog. Mater. Sci.* **131**, 101003 (2023).
11. Gao, M. et al. Power generation for wearable systems. *Energy Environ. Sci.* **14**, 2114–2157 (2021).
12. Cao, T., Shi, X.-L., Zou, J. & Chen, Z.-G. Advances in conducting polymer-based thermoelectric materials and devices. *Microstructures* **1**, 2021007 (2021).
13. Lu, Y. et al. Staggered-layer-boosted flexible Bi₂Te₃ films with high thermoelectric performance. *Nat. Nanotechnol.* **18**, 1281–1288 (2023).
14. Zheng, Z.-H. et al. Harvesting waste heat with flexible Bi₂Te₃ thermoelectric thin film. *Nat. Sustain.* **6**, 180–191 (2023).
15. Wu, H., Shi, X.-L., Duan, J., Liu, Q. & Chen, Z.-G. Advances in Ag₂Se-based thermoelectrics from materials to applications. *Energy Environ. Sci.* **16**, 1870–1906 (2023).
16. Yang, D. et al. Flexible power generators by Ag₂Se thin films with record-high thermoelectric performance. *Nat. Commun.* **15**, 923 (2024).

17. Tang, X., Li, Z., Liu, W., Zhang, Q. & Uher, C. A comprehensive review on Bi₂Te₃-based thin films: Thermoelectrics and beyond. *Interdiscipl. Mater.* **1**, 88–115 (2022).
18. Qin, H. et al. Critical role of tellurium self-compensation in enhancing the thermoelectric performance of p-Type Bi_{0.4}Sb_{1.6}Te₃ alloy. *Chem. Eng. J.* **425**, 130670 (2021).
19. Liu, Z.-Y., Zhu, J.-L., Tong, X., Niu, S. & Zhao, W.-Y. A review of CoSb₃-based skutterudite thermoelectric materials. *J. Adv. Ceram.* **9**, 647–673 (2020).
20. He, J. & Tritt, T. M. Advances in thermoelectric materials research: looking back and moving forward. *Science* **357**, eaak9997 (2017).
21. Sales, B. C., Mandrus, D., Chakoumakos, B. C., Keppens, V. & Thompson, J. R. Filled skutterudite antimonides: Electron crystals and phonon glasses. *Phys. Rev. B* **56**, 15081–15089 (1997).
22. Nolas, G. S., Morelli, D. T. & Tritt, T. M. SKUTTERUDITES: A phonon-glass-electron crystal approach to advanced thermoelectric energy conversion applications. *Annu. Rev. Mater. Sci.* **29**, 89–116 (1999).
23. Li, D. et al. Fast fabrication of high-performance CoSb₃-based thermoelectric skutterudites via one-step Yb-promoted peritectic solidification. *Adv. Funct. Mater.* **33**, 2305269 (2023).
24. Daniel, M. V. et al. Structural and thermoelectric properties of FeSb₃ skutterudite thin films. *Phys. Rev. B* **91**, 085410 (2015).
25. Bourgès, C. et al. Drastic power factor improvement by Te doping of rare earth-free CoSb₃-skutterudite thin films. *RSC Adv.* **10**, 21129–21135 (2020).
26. Li, D. et al. Ce-filled Ni_{1.5}Co_{2.5}Sb₁₂ skutterudite thin films with record-high figure of merit and device performance. *Adv. Energy Mater.* **13**, 2301525 (2023).
27. Zheng, Z.-h et al. Thermoelectric properties and micro-structure characteristics of nano-sized CoSb₃ thin films prefabricating by co-sputtering. *J. Alloy. Compd.* **732**, 958–962 (2018).
28. Masarrat, A. et al. Effect of Fe ion implantation on the thermoelectric properties and electronic structures of CoSb₃ thin films. *RSC Adv.* **9**, 36113–36122 (2019).
29. Liang, G.-x et al. Nano structure Ti-doped skutterudite CoSb₃ thin films through layer inter-diffusion for enhanced thermoelectric properties. *J. Eur. Ceram. Soc.* **39**, 4842–4849 (2019).
30. Yadav, S., Yadav, B. S., Chaudhary, S. & Pandya, D. K. Deposition potential controlled structural and thermoelectric behavior of electrodeposited CoSb₃ thin films. *RSC Adv.* **7**, 20336–20344 (2017).
31. Bala, M. et al. Evolution of nanostructured single-phase CoSb₃ thin films by low-energy ion beam induced mixing and their thermoelectric performance. *Phys. Chem. Chem. Phys.* **19**, 24886–24895 (2017).
32. Yang, Y. J. et al. Thermoelectric properties of CoSb₃ nanoparticle films. *Adv. Mater. Res.* **347-353**, 3448–3455 (2012).
33. Latronico, G. et al. Effect of the annealing treatment on structural and transport properties of thermoelectric Sm_y(Fe_xNi_{1-x})₄Sb₁₂ thin films. *Nanotechnology* **34**, 115705 (2023).
34. Suzuki, A. Pulsed laser deposition of filled skutterudite LaFe₃CoSb₁₂ thin films. *Jpn. J. Appl. Phys.* **42**, 2843 (2003).
35. Zeipl, R. et al. Properties of thin n-type Yb_{0.14}Co₄Sb₁₂ and p-type Ce_{0.09}Fe_{0.67}Co_{3.33}Sb₁₂ skutterudite layers prepared by laser ablation. *J. Vac. Sci. Technol. A* **28**, 523–527 (2010).
36. Caylor, J. C., Stacy, A. M., Gronsky, R. & Sands, T. Pulsed laser deposition of skutterudite thin films. *J. Appl. Phys.* **89**, 3508–3513 (2001).
37. Arnache, O. et al. Electrical and structural properties of Ce_{0.9}CoFe₃Sb₁₂ thermoelectric thin films. *Solid State Commun.* **133**, 343–346 (2005).
38. Tan, G., Wang, S., Li, H., Yan, Y. & Tang, X. Enhanced thermoelectric performance in zinc substituted p-type filled skutterudites CeFe_{4-x}Zn_xSb₁₂. *J. Solid State Chem.* **187**, 316–322 (2012).
39. Tan, G. et al. Rapid preparation of CeFe₄Sb₁₂ skutterudite by melt spinning: rich nanostructures and high thermoelectric performance. *J. Mater. Chem. A* **1**, 12657–12668 (2013).
40. Tang, X. F., Chen, L. D., Goto, T., Hirai, T. & Yuan, R. Z. Synthesis and thermoelectric properties of p-type barium-filled skutterudite Ba_yFe_xCo_{4-x}Sb₁₂. *J. Mater. Res.* **17**, 2953–2959 (2002).
41. Son, G. et al. Control of electrical to thermal conductivity ratio for p-type La_xFe₃CoSb₁₂ thermoelectrics by using a melt-spinning process. *J. Alloy. Compd.* **729**, 1209–1214 (2017).
42. Bae, S. H., Lee, K. H. & Choi, S.-M. Effective role of filling fraction control in p-type Ce_xFe₃CoSb₁₂ skutterudite thermoelectric materials. *Intermetallics* **105**, 44–47 (2019).
43. Qiu, P. et al. Enhancement of thermoelectric performance in slightly charge-compensated Ce_yCo₄Sb₁₂ skutterudites. *Appl. Phys. Lett.* **103**, 062103 (2013).
44. Tang, Y., Hanus, R., Chen, S.-W. & Snyder, G. J. Solubility design leading to high figure of merit in low-cost Ce-CoSb₃ skutterudites. *Nat. Commun.* **6**, 7584 (2015).
45. Wan, S., Huang, X., Qiu, P., Bai, S. & Chen, L. The effect of short carbon fibers on the thermoelectric and mechanical properties of p-type CeFe₄Sb₁₂ skutterudite composites. *Mater. Des.* **67**, 379–384 (2015).
46. Tong, X. et al. Research progress of p-type Fe-based skutterudite thermoelectric materials. *Front. Mater. Sci.* **15**, 317–333 (2021).
47. Liu, Z. et al. Alloying engineering for thermoelectric performance enhancement in p-type skutterudites with synergistic carrier concentration optimization and thermal conductivity reduction. *J. Adv. Ceram.* **12**, 539–552 (2023).
48. Ding, J. et al. Selenium-substituted diketopyrrolopyrrole polymer for high-performance p-type organic thermoelectric materials. *Angew. Chem. Int. Ed.* **58**, 18994–18999 (2019).
49. Imae, I., Goto, T., Ooyama, Y. & Harima, Y. Thermoelectric properties of poly(3,4-ethylenedioxythiophene) with fluorine-containing polyanion as dopant. *Polymer* **199**, 122538 (2020).
50. Wang, H. & Yu, C. Organic thermoelectrics: materials preparation, performance optimization, and device integration. *Joule* **3**, 53–80 (2019).
51. Xia, Z.-X. et al. Enhancement effect of the C₆₀ derivative on the thermoelectric properties of n-type single-walled carbon nanotube-based films. *ACS Appl. Mater. Interfaces* **14**, 54969–54980 (2022).
52. Jin, Q. et al. Flexible layer-structured Bi₂Te₃ thermoelectric on a carbon nanotube scaffold. *Nat. Mater.* **18**, 62–68 (2019).
53. Chen, X. et al. Flexible thermoelectric films based on Bi₂Te₃ nanosheets and carbon nanotube network with high n-type performance. *ACS Appl. Mater. Interfaces* **13**, 5451–5459 (2021).
54. Rongione, N. A. et al. High-performance solution-processable flexible SnSe nanosheet films for lower grade waste heat recovery. *Adv. Electron. Mater.* **5**, 1800774 (2019).
55. Li, Y. et al. Enhanced thermoelectric properties of Cu₂Se flexible thin films by optimizing growth temperature and elemental composition. *ACS Appl. Energy Mater.* **5**, 13964–13970 (2022).
56. Ding, Y. et al. High performance n-type Ag₂Se film on nylon membrane for flexible thermoelectric power generator. *Nat. Commun.* **10**, 841 (2019).
57. Ao, D.-W. et al. Assembly-free fabrication of high-performance flexible inorganic thin-film thermoelectric device prepared by a thermal diffusion. *Adv. Energy Mater.* **12**, 2202731 (2022).
58. Lu, Y. et al. Ultrahigh power factor and flexible silver selenide-based composite film for thermoelectric devices. *Energy Environ. Sci.* **13**, 1240–1249 (2020).
59. Wei, M. et al. Directional thermal diffusion realizing inorganic Sb₂Te₃/Te hybrid thin films with high thermoelectric performance and flexibility. *Adv. Funct. Mater.* **32**, 2207903 (2022).
60. Zang, J. et al. Effect of post-annealing treatment on the thermoelectric properties of Ag₂Se flexible thin film prepared by magnetron sputtering method. *Res. Phys.* **45**, 106222 (2023).

61. Kato, A. et al. Facile fabrication of n-type flexible $\text{CoSb}_{3-x}\text{Te}_x$ skutterudite/PEDOT:PSS hybrid thermoelectric films. *Polymers* **14**, 1986 (2022).
62. Shang, H. et al. High-performance Ag-modified $\text{Bi}_{0.5}\text{Sb}_{1.5}\text{Te}_3$ films for the flexible thermoelectric generator. *ACS Appl. Mater. Interfaces* **12**, 7358–7365 (2020).
63. Varghese, T. et al. Flexible thermoelectric devices of ultrahigh power factor by scalable printing and interface engineering. *Adv. Funct. Mater.* **30**, 1905796 (2020).
64. Shang, H. et al. $\text{Bi}_{0.5}\text{Sb}_{1.5}\text{Te}_3$ -based films for flexible thermoelectric devices. *J. Mater. Chem. A* **8**, 4552–4561 (2020).
65. Kong, D., Zhu, W., Guo, Z. & Deng, Y. High-performance flexible Bi_2Te_3 films based wearable thermoelectric generator for energy harvesting. *Energy* **175**, 292–299 (2019).
66. Jin, Q. et al. Cellulose fiber-based hierarchical porous bismuth telluride for high-performance flexible and tailorable thermoelectrics. *ACS Appl. Mater. Interfaces* **10**, 1743–1751 (2018).
67. Komatsu, N. et al. Macroscopic weavable fibers of carbon nanotubes with giant thermoelectric power factor. *Nat. Commun.* **12**, 4931 (2021).
68. Warrender, J. M. & Aziz, M. J. Kinetic energy effects on morphology evolution during pulsed laser deposition of metal-on-insulator films. *Phys. Rev. B* **75**, 085433 (2007).
69. Warrender, J. M. & Aziz, M. J. Evolution of Ag nanocrystal films grown by pulsed laser deposition. *Appl. Phys. A* **79**, 713–716 (2004).
70. Li, X.-G. et al. Ce filling limit and its influence on thermoelectric performance of $\text{Fe}_3\text{CoSb}_{12}$ -based skutterudite grown by a temperature gradient zone melting method. *Materials* **14**, 6810 (2021).
71. Li, X.-G. et al. Impurity removal leading to high-performance CoSb_3 -based skutterudites with synergistic carrier concentration optimization and thermal conductivity reduction. *ACS Appl. Mater. Interfaces* **13**, 54185–54193 (2021).
72. Li, D., Li, S., Li, X., Yang, B. & Zhong, H. Efficiently synthesized n-type CoSb_3 thermoelectric alloys under TGZM effect. *Mat. Sci. Semicon. Proc.* **123**, 105542 (2021).
73. Song, D. W. et al. Thermal conductivity of skutterudite thin films and superlattices. *Appl. Phys. Lett.* **77**, 3854–3856 (2000).
74. Savchuk, V., Boulouz, A., Chakraborty, S., Schumann, J. & Vinzelberg, H. Transport and structural properties of binary skutterudite CoSb_3 thin films grown by dc magnetron sputtering technique. *J. Appl. Phys.* **92**, 5319–5326 (2002).
75. He, H. et al. Temperature-arousing self-powered fire warning e-textile based on p–n segment coaxial aerogel fibers for active fire protection in firefighting clothing. *Nano-Micro Lett.* **15**, 226 (2023).
76. Jiang, C. et al. A high-thermopower ionic hydrogel for intelligent fire protection. *J. Mater. Chem. A* **10**, 21368–21378 (2022).
77. Zhao, Y. et al. Self-powered, durable and high fire-safety ionogel towards Internet of Things. *Nano Energy* **116**, 108785 (2023).
78. Li, G. et al. Thermoelectric and photoelectric dual modulated sensors for human internet of things application in accurate fire recognition and warning. *Adv. Funct. Mater.* **33**, 2303861 (2023).
79. Wang, H., Li, S., Li, X. & Zhong, H. Microstructure and thermoelectric properties of doped p-type CoSb_3 under TGZM effect. *J. Cryst. Growth* **466**, 56–63 (2017).
80. Li, X. et al. Effect of hot pressing on the microstructure and thermoelectric properties of TGZM-grown YbFe-doped CoSb_3 skutterudite. *Ceram. Int.* **47**, 8949–8958 (2021).
81. Wang, H. et al. Thermoelectric transport effects beyond single parabolic band and acoustic phonon scattering. *Mater. Adv.* **3**, 734–755 (2022).
82. Shi, X.-L. et al. Optimization of sodium hydroxide for securing high thermoelectric performance in polycrystalline Sn_{1-x}Se via anisotropy and vacancy synergy. *InfoMat* **2**, 1201–1215 (2020).

Acknowledgements

This work was supported by the Research Fund of the National Natural Science Foundation of China (51774239), and the Research Fund of the State Key Laboratory of Solidification Processing in NWPU (2022-TS-03). Zhi-Gang Chen thanks the financial support from the Australian Research Council, HBIS-UQ Innovation Centre for Sustainable Steel project, and QUT Capacity Building Professor Program. Zhigang Chen and Meng Li acknowledge the National Computational Merit Allocation Scheme 2024 (wk98), sponsored by National Computational Infrastructure, for providing computational resources and services. This work was enabled by the use of the Central Analytical Research Facility hosted by the Institute for Future Environments at QUT.

Author contributions

D.Li & X.-L.Shi contributed equally to this work. Z.-G.Chen, S.-M.Li and H.Zhong supervised the project and conceived the idea. D.Li and X.-L.Shi designed the experiments and wrote the manuscript. D.Li, J.-X.Zhu, Z.-K.Han, Z.-Y.Feng, Y.-X.Chen and J.-Y.Wang performed the sample synthesis, structural characterization, and thermoelectric transport property measurements. M.Li and X.-L.Shi undertook the theoretical work. J.-X.Zhu and X.Ma conducted the TEM measurements and T.-Y.Cao conducted the measurement of the in-plane κ of the films. X.-L.Shi, M.Li, W.-D.Liu, Z.-G.Chen, and S.-M.Li undertook the thermoelectric performance evaluation. All the authors discussed the results and commented on the manuscript. All authors have approved the final version of the manuscript.

Competing interests

The authors declare no competing interests.

Additional information

Supplementary information The online version contains supplementary material available at <https://doi.org/10.1038/s41467-024-48677-4>.

Correspondence and requests for materials should be addressed to Hong Zhong, Shuangming Li or Zhi-Gang Chen.

Peer review information *Nature Communications* thanks the anonymous reviewer(s) for their contribution to the peer review of this work. A peer review file is available.

Reprints and permissions information is available at <http://www.nature.com/reprints>

Publisher's note Springer Nature remains neutral with regard to jurisdictional claims in published maps and institutional affiliations.

Open Access This article is licensed under a Creative Commons Attribution 4.0 International License, which permits use, sharing, adaptation, distribution and reproduction in any medium or format, as long as you give appropriate credit to the original author(s) and the source, provide a link to the Creative Commons licence, and indicate if changes were made. The images or other third party material in this article are included in the article's Creative Commons licence, unless indicated otherwise in a credit line to the material. If material is not included in the article's Creative Commons licence and your intended use is not permitted by statutory regulation or exceeds the permitted use, you will need to obtain permission directly from the copyright holder. To view a copy of this licence, visit <http://creativecommons.org/licenses/by/4.0/>.

© The Author(s) 2024